

## Article

# Seamless Switching Control Strategy for a Power Conversion System in a Microgrid Based on Extended State Observer and Super-Twisting Algorithm

Jiayu Kang <sup>\*</sup>, Ye Wang <sup>\*</sup>, Jiachen Wang and Baoquan Liu

School of Electrical and Control Engineering, Shaanxi University of Science and Technology, Xi'an 710021, China; 210612081@sust.edu.cn (J.W.); liubq@sust.edu.cn (B.L.)

<sup>\*</sup> Correspondence: kangjiayu@sust.edu.cn (J.K.); 210612089@sust.edu.cn (Y.W.)

**Abstract:** Microgrids can operate stably in both islanded and grid-connected modes, and the transition between these modes enhances system reliability and flexibility, enabling microgrids to adapt to diverse operational requirements and environmental conditions. The switching process, however, may introduce transient voltage and frequency fluctuations, causing voltage and current shocks to the grid and potentially damaging devices and systems connected to the microgrid. To address this issue, this study introduces a novel approach based on the Extended State Observer (ESO) and the Super-Twisting Algorithm (STA). Power conversion systems use Virtual Synchronous Generator (VSG) control and Power-Quality (PQ) control when they are connected to the grid or when the microgrid is not connected to the grid. VSG and PQ share a current loop. Transitioning the reference current generated by the outer loop achieves the switching of control strategies. A real-time observer is designed to estimate and compensate for current fluctuations, disturbances, and variations in  $i_d$ ,  $i_q$ , and system parameters during the switching process to facilitate a smooth transition of control strategies. Furthermore, to enhance the dynamic response and robustness of the system, the Proportional–Integral (PI) controller in the ESO is replaced with a novel super-twisting sliding mode controller based on a boundary layer. The Lyapunov stability principle is applied to ensure asymptotic stability under disturbances. The proposed control strategy is validated through simulation using a seamless switching model of the power conversion system developed on the Matlab/Simulink (R2021b) platform. Simulation results demonstrate that the optimized control strategy enables smooth microgrid transitions, thereby improving the overall reliability of grid operations.



**Citation:** Kang, J.; Wang, Y.; Wang, J.; Liu, B. Seamless Switching Control Strategy for a Power Conversion System in a Microgrid Based on Extended State Observer and Super-Twisting Algorithm. *Electronics* **2024**, *13*, 1708. <https://doi.org/10.3390/electronics13091708>

Academic Editor: Carlos Andrés García-Vázquez

Received: 29 February 2024

Revised: 18 April 2024

Accepted: 24 April 2024

Published: 29 April 2024



**Copyright:** © 2024 by the authors. Licensee MDPI, Basel, Switzerland. This article is an open access article distributed under the terms and conditions of the Creative Commons Attribution (CC BY) license (<https://creativecommons.org/licenses/by/4.0/>).

## 1. Introduction

As the assimilation of renewable energy sources such as wind and solar into the power grid continues to increase, the large-scale integration of distributed energy into the distribution network is expected to have adverse effects on the stability of the grid. Energy storage plays a crucial role in reducing the fluctuations of distributed energy sources, enhancing system stability and being pivotal in the operation of microgrids [1]. The capability of microgrids to operate in both islanded and grid-connected modes is advantageous, and mitigating the impacts during mode transitions is a key focus in microgrid research [2]. Due to the inherent variability of renewable energy generation, Power Conversion Systems (PCSSs) in energy storage inverters are required not only to provide active and reactive power to the main grid during grid-connected conditions, but also to stabilize voltage and frequency in islanded mode. The coordinated control of PCSSs is crucial for ensuring the stable operation and smooth transition of microgrids [3–5], highlighting the necessity for research on control strategies.

To achieve smooth operation and seamless transition in microgrids, researchers have employed various control strategies to enhance system stability. By simulating the mechanical structure of a synchronous generator, Virtual Synchronous Generator (VSG) control imparts system inertia and damping, thereby enhancing the robustness of microgrid systems [6,7]. It plays a crucial role in stabilizing voltage and balancing power in power systems. To address voltage fluctuations and current shocks during microgrid transitions, researchers have extensively studied switching control. These methods are generally divided into two types. The first involves improving the VSG algorithm parameters' adaptability to disturbances during the switching process. The second section focuses on improving inverter control performance.

A study [8] compared VSG/PQ control with droop control, where VSG/PQ showed better results but the switching-induced current shocks were significant. Another study [9] proposed an improved voltage loop control structure based on VSG control, achieving a smooth transition from grid-connected to islanded mode. However, simulation results indicated residual current distortion during the transition. A strategy for seamless switching control with shared current loops for VSG and PQ was proposed in [10], adjusting the weight of current references from both control strategies for seamless transition. However, weight settings led to prolonged adjustment times. Studies [11,12] presented a parallel switching method based on a numerical buffer for VSG/PQ, achieving smooth transitions between microgrid-islanded and grid-connected operations. Another study [13] utilized a state follower to track controller outputs in both modes, achieving smooth transitions but with minor voltage and current fluctuations. To achieve zero steady-state tracking errors and improve response speed and robustness, ref. [14] introduced a third-order sliding mode control with a saturation function replacing the sign function. However, the saturation function is discontinuous and not differentiable, affecting its ability to track sudden changes during grid transition. The super-twisting sliding mode algorithm is a continuous alternative, but the existence of discrete steps and sign functions can still result in chattering. Ref. [15] utilized the super-twisting algorithm for controlling grid-connected inverters, making the control signal continuous to reduce chattering, but did not consider off-grid operation or the system's stability during transitions. Ref. [16] optimized the super-twisting algorithm using a saturation function, but the boundary layer problem became another limiting factor, requiring a comprehensive consideration of control accuracy and chattering elimination.

Building upon the existing research on seamless transitions in microgrids, this paper proposes a seamless switching control strategy for PCS based on VSG/PQ. Building upon VSG/PQ switching, the VSG and PQ share the inner current loop, achieving control strategy transitions by switching the outer loop current command. This ensures synchronicity between the control strategy switch and the Point of Common Coupling (PCC) switch moment. To fix the small changes in voltage and current that happen when current commands are suddenly changed, a super-twisting sliding mode controller is being built to replace the traditional current inner loop. This will make the system more stable and responsive, ensuring that the microgrid works well and responds quickly. Finally, an improved boundary saturation function is designed to optimize the super-twisting algorithm. By employing different convergence strategies inside and outside the boundary layer, the system's chattering is weakened, improving dynamic response performance and achieving smooth transitions.

## 2. Modeling of the Inverter

As shown in Figure 1, the microgrid system mainly consists of primary equipment such as a photovoltaic power generation system, energy storage system, and load, as well as secondary equipment for measurement, monitoring, and protection. The alternating current (AC) bus is connected to the large power grid by the grid-connected switch. There are many operation modes in the micro-grid, such as off-grid operation, grid-connected operation, and pre-synchronous operation.

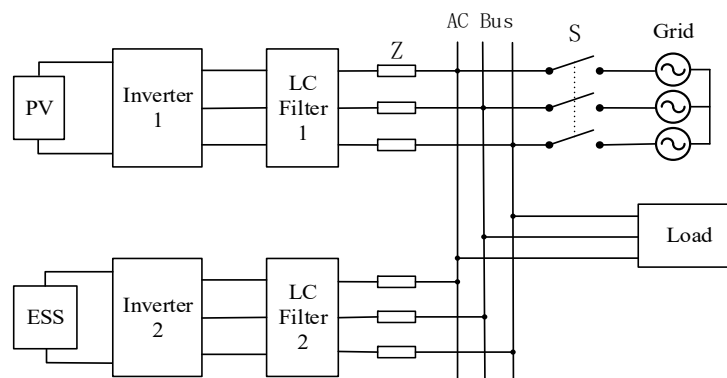


**Figure 1.** Structure of the photovoltaic storage microgrid.

When there are many distributed power sources in the micro-grid, the control mode can be divided into master-slave, peer-to-peer, and hierarchical control. Because of the uncertainty of photovoltaic power generation, its power output has a large fluctuation, so the energy storage system can be used as the main control unit and the photovoltaic power generation system as a subordinate control unit.

The configuration of the PCS in a microgrid is depicted in Figure 2. When the switch CB at the PCC is closed, the PCS operates in grid-connected mode, employing constant PQ control. In the event of the CB switch being open, the energy inverter assumes the role of a voltage source in islanded mode, utilizing VSG control to provide voltage and frequency support. In the diagram,  $U_{dc}$  denotes the direct current (DC) source voltage, and  $S_1 \sim S_6$  represent the switch devices, collectively forming a three-phase inverter.  $R$ ,  $L$ , and  $C$  signify the equivalent resistance, inductance, and capacitance of the filtering circuit.  $P_0$  and  $Q_0$  represent the actual active and reactive power output of the inverter, while  $P_{ref}$  and  $Q_{ref}$  are the predetermined references for active and reactive power.  $u_k$  and  $i_k$  represent the measured AC voltage and inductor current of the inverter,  $u_{ok}$  and  $i_{ok}$  are the voltage (capacitor voltage) at the PCC and the filtered current, and  $u_{gk}$  is the voltage of the main grid. Here,  $k = a, b$ , and  $c$ .

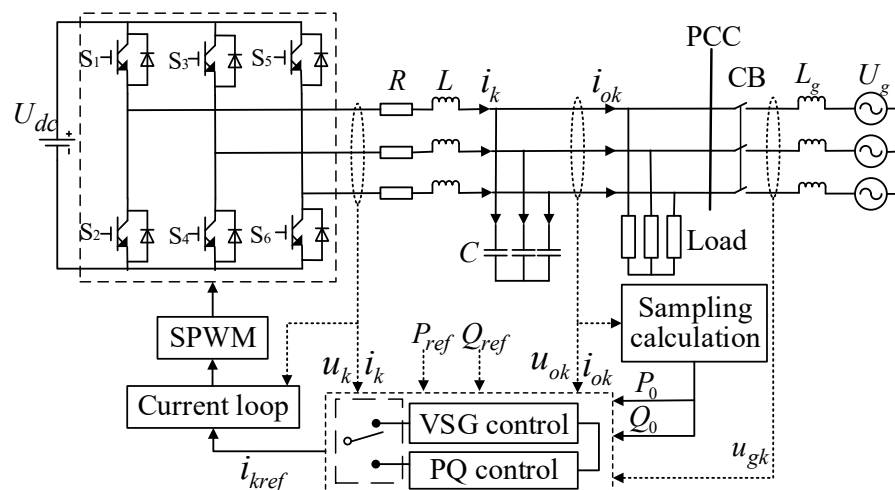


**Figure 2.** Control structure of Power Conversion System.

Kirchhoff's voltage law is used to set up the current state equations for the PCS in the  $d$ - $q$  rotating coordinate system for the main circuit shown in Figure 2. The current state equations for the PCS can be formulated as follows using the  $d$ - $q$  coordinate system:

$$\begin{cases} \frac{di_d}{dt} = -\frac{R}{L}i_d + \omega i_q + \frac{1}{L}u_d - \frac{1}{L}u_{od} \\ \frac{di_q}{dt} = -\frac{R}{L}i_q - \omega i_d + \frac{1}{L}u_q - \frac{1}{L}u_{oq} \end{cases} \quad (1)$$

where  $u_d = U_{dc} * S_d$ ,  $u_q = U_{dc} * S_q$ ,  $i_d$ , and  $i_q$  are the  $d$ - $q$  axis components of the inductor current (A),  $u_d$  and  $u_q$  represent the  $d$ - $q$  axis components of the inverter's AC output voltage (V),  $u_{od}$  and  $u_{oq}$  are the  $d$ - $q$  axis components of the capacitor voltage (V), and  $\omega$  is the angular frequency, while  $S_d$  and  $S_q$  denote the  $d$ - $q$  axis components of the switch control signals.

Figure 3 shows the traditional current inner-loop decoupling control based on Equation (1). The PI controller for the current inner loop is shown by  $k_I(s)$ . Voltage feedforward compensation is used at the output of the current compensator to lessen the effect that the output voltage has on the current inner loop output. Consequently, the output current is influenced not only by the current reference value but also by disturbances from the output voltage.

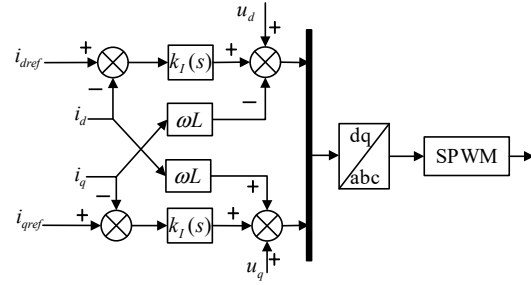


**Figure 3.** Current control block diagram with voltage feedforward compensation.

### 3. Power Conversion System Control Strategy

#### 3.1. VSG Control Strategy

The second-order model of an implicit-pole synchronous generator with a pole pair number of 1 has been studied as an example [17,18]. This was undertaken to avoid the complexity of electromagnetic coupling in synchronous motors. When the pole pair number is 1, the generator's power angle  $\delta$  is equal to the phase angle  $\theta$ . The virtual synchronous machine's torque is composed of three parts: the mechanical torque from the prime mover, the electromagnetic torque from the synchronous generator to itself, and the damping torque, denoted as  $T_m$ ,  $T_e$ , and  $T_D$ , respectively [19]. The system's rotational inertia  $J$  and damping coefficient  $D$  impart inertia and damping. The mechanical power  $P_m$  and electromagnetic power  $P_e$  are obtained by calculating the mechanical and electromagnetic torques, and the rotor angular velocity  $\omega$  continuously approaches the rated value  $\omega_0$ . The rotor mechanical equation for the virtual synchronous generator is established:

$$\begin{cases} J \frac{d(\omega - \omega_0)}{dt} = T_m - T_e - T_D = \frac{P_m}{\omega_0} - \frac{P_e}{\omega} - D(\omega - \omega_0) \\ \omega = \frac{d\delta}{dt} = \frac{d\theta}{dt} \end{cases} \quad (2)$$

The  $P$ - $f$  controller provides electromagnetic torque by simulating the active droop characteristic of a synchronous generator. Set reference active power  $P_{ref}$  and droop active power  $\Delta P$  determine the mechanical power  $P_m$ .

$$P_m = P_{ref} + \Delta P = P_{ref} + K_p(\omega_0 - \omega) \quad (3)$$

The  $Q$ - $U$  controller adjusts the reactive power based on the droop characteristic. The VSG no-load potential  $U_n$ , the set reference reactive power  $Q_{ref}$ , and the droop reactive power  $\Delta Q$  determine the amplitude reference value of the terminal voltage  $E$ .

$$E = (K_p + \frac{K_i}{s})[U_n + K_Q(Q_{ref} - Q)] \quad (4)$$

The stator voltage equation determines the synchronous generator's virtual stator impedance. The excitation voltage is calculated through the impedance drop, providing a

reference voltage for the voltage inner loop. The stator voltage equation for the synchronous generator can be established as follows:

$$u_{ref} = E - i(r_a + jX_d) \quad (5)$$

where  $u_{ref}$  is the reference voltage obtained by the upper layer VSG algorithm at the inverter port,  $i$  is the stator armature current, and  $r_a$  and  $X_d$  together form the virtual impedance. Different impedance drop values can be set to improve dynamic characteristics. In this study, the armature resistance is set to 0 and the synchronous reactance is set to  $\omega_{Ls}$ .

The block diagram of the VSG controller can be obtained from Equations (2) to (5), as illustrated in Figure 4.

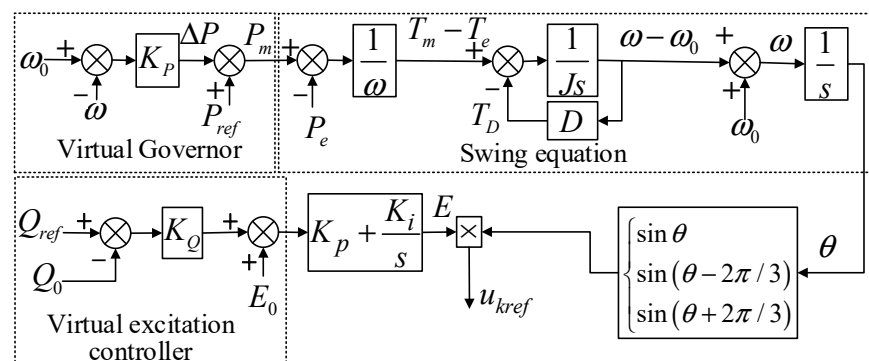


**Figure 4.** Power loop control structure based on virtual synchronization.

The voltage loop maintains actual voltage stability by tracking the voltage reference generated by the VSG power loop. Decoupling is required for independent control because of the coupling of the inverter output three-phase voltages and the mutual coupling of the current [20]. The voltage loop state equations for the PCS in the  $d$ - $q$  rotating coordinate system can be established according to Kirchhoff's current law and in conjunction with Figure 1:

$$\begin{cases} \frac{du_{od}}{dt} = \frac{1}{C}i_{od} - \frac{1}{C}i_{oq} + \omega u_{oq} \\ \frac{du_{oq}}{dt} = \frac{1}{C}i_{oq} - \frac{1}{C}i_{od} + \omega u_{od} \end{cases} \quad (6)$$

where  $i_{od}$  and  $i_{oq}$  are the  $d$ - $q$  axis components of the filtered current (A). PI control is employed to regulate the voltage, generating a reference current as the input signal for the current inner loop. The expression for the voltage loop is obtained as follows:

$$\begin{cases} i_{VSGd} = (u_{dref} - u_{od})\left(k_p + \frac{k_i}{s}\right) + i_{od} - \omega Cu_{oq} \\ i_{VSGq} = (u_{qref} - u_{oq})\left(k_p + \frac{k_i}{s}\right) + i_{oq} + \omega Cu_{od} \end{cases} \quad (7)$$

where  $i_{VSGd}$  and  $i_{VSGq}$  are the  $d$ - $q$  axis components of the VSG output reference current (A),  $u_{dref}$  and  $u_{qref}$  are the  $d$ - $q$  axis components of the VSG output reference voltage (V), and  $k_p$  and  $k_i$  are the proportional and integral coefficients of the PI controller.

### 3.2. PQ Control Strategy

When there is a significant voltage or frequency deviation between the microgrid and the grid, VSG control may lead to overloading of the PCS due to the limited energy storage capacity of the energy storage module, causing voltage and frequency oscillations in the microgrid. The system selects the PQ control strategy to meet the power output requirements during grid-connected operation. Its control principle is as follows: using the voltage and frequency of the main grid as references, it maintains the voltage amplitude and frequency of the microgrid to roughly follow the operation of the main grid. The main control system adjusts the current magnitude and phase based on power demand. PQ control consists of a power outer loop and a current inner loop; the power outer loop

determines the reference current, which serves as the input signal for the inner loop. The inverter output reference power is determined by

$$\begin{cases} P_{ref} = \frac{3}{2}(u_{gd}i_{PQd} + u_{gq}i_{PQq}) \\ Q_{ref} = \frac{3}{2}(u_{gd}i_{PQq} - u_{gq}i_{PQd}) \end{cases} \quad (8)$$

where  $i_{PQd}$  and  $i_{PQq}$  are the  $d$ - $q$  axis components of the reference current output by the PQ control power loop (A), and  $u_{gd}$  and  $u_{gq}$  are the  $d$ - $q$  axis components of the three-phase grid voltage (V). In the ideal rotating coordinate system, the  $q$ -axis component of the grid voltage is 0. Hence, the expression for the power loop is derived as follows:

$$\begin{cases} i_{PQd} = \frac{2}{3} \frac{P_{ref}}{u_{gd}} \\ i_{PQq} = -\frac{2}{3} \frac{Q_{ref}}{u_{gd}} \end{cases} \quad (9)$$

### 3.3. Switch Control Strategy

During prolonged islanded operation of the microgrid, power influences the output voltage, leading to deviations in amplitude, phase, and frequency compared to the main grid. Attempting grid connection directly when significant deviations occur may result in substantial impact currents, leading to grid connection failure and even causing grid oscillations, posing safety hazards. Taking the example of the a-phase of three-phase symmetrical voltages under normal conditions, let the microgrid bus voltage be  $u_{oa} \angle \theta$  and the grid voltage be  $u_{ga} \angle \theta_g$ , with the difference between them denoted as  $u$ . Generally, the amplitude  $U_o$  of the microgrid bus voltage is almost identical to the amplitude  $U_g$  of the main grid voltage, but there may be a significant phase difference. Therefore,

$$\begin{aligned} \Delta u &= u_{oa} - u_{ga} \\ &= U_o \sin(\omega t + \theta) - U_g \sin(\omega_0 t + \theta_g) \\ &\approx 2U \sin\left(\frac{\omega - \omega_0}{2}t + \frac{\theta - \theta_g}{2}\right) \cos\left(\frac{\omega + \omega_0}{2}t + \frac{\theta + \theta_g}{2}\right) \end{aligned} \quad (10)$$

Even if the amplitude of the microgrid bus voltage is close to the grid voltage amplitude, due to the existence of a phase difference, a maximum voltage difference of  $2U$  occurs on both sides of the PCC point during grid connection, leading to significant impact currents causing grid oscillations and switch failures. Therefore, pre-synchronization control is employed before grid connection to compensate for both amplitude and phase, making the inverter output voltage approach the grid voltage, thereby reducing grid connection impacts.

$$\begin{cases} E = E^* + \Delta E_s = E^* + \frac{K_E}{s}(u_g - u_o) \\ \omega = \omega^* + \Delta \omega_s = \omega^* + \frac{K_\omega}{s}(\theta_g - \theta) \end{cases} \quad (11)$$

where  $E$  is the reference voltage amplitude,  $E^*$  is the reference voltage amplitude before compensation, and the amplitude integral coefficient  $K_E$  adjusts the amplitude to be consistent with the grid voltage amplitude.  $\omega^*$  is the angular frequency before phase compensation, and the phase integral coefficient  $K_\omega$  adjusts the phase to approach the grid frequency. The control block diagram for the pre-synchronization strategy is shown in Figure 5.

During the islanded operation of the microgrid, the amplitude and phase compensation switches,  $S$ , remain open. Upon receiving the pre-synchronization signal, the switch  $S$  closes, initiating pre-synchronization control to adjust the voltage amplitude  $E$  and phase  $\theta$ . Upon meeting the conditions for grid connection, the system immediately initiates grid connection by opening switch  $S$ .

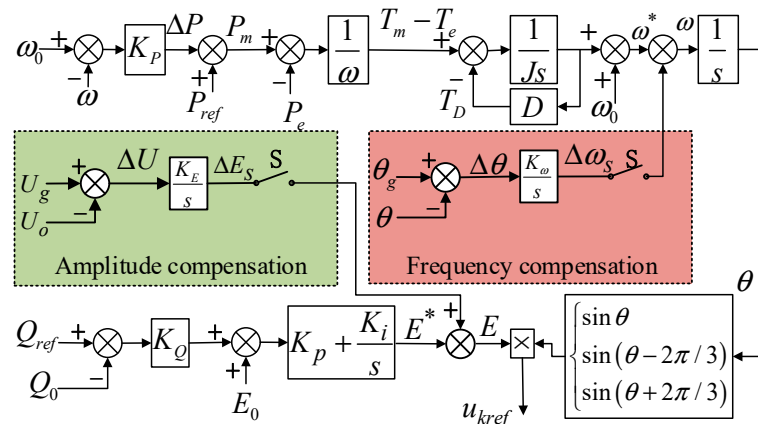


**Figure 5.** Pre-synchronization control block diagram.

This paper integrates the advantages of VSG control and PQ control, allowing VSG and PQ to run in parallel, and the control strategy must synchronize switching during the instantaneous mode transition. Both control strategies involve current loops in their inner structures upon analysis of their principles. To minimize the impact of mode transitions, this paper enables both control strategies to run simultaneously and share a common current loop. Switching the control method involves toggling the current reference signals generated by the two control strategies, as illustrated in Figure 6, where  $i_{dref}$  and  $i_{qref}$  represent the  $d$ - $q$  axis components (A) of the inner loop input current reference values.

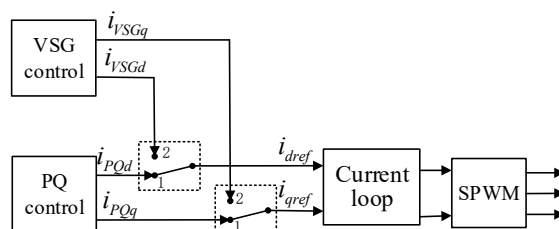


**Figure 6.** VSG/PQ switching control diagram.

#### 4. Super-Twisting Algorithm Based on Extended State Observer

The current inner loop regulates the inductance current based on the reference current. In conventional VSG/PQ switching, a discontinuity in  $i_{ref}$  occurs due to the difference between  $i_{VSG}$  and  $i_{PQ}$ , leading to significant transient fluctuations in the inverter's AC-side voltage and frequency. Moreover, even after meeting the conditions for grid connection, there may still be deviations in voltage amplitude, frequency, and phase. At this point, an immediate grid connection can result in significant shock currents. Designing an ESO to dynamically observe  $i_d$  and  $i_q$  achieves a smooth transition. Real-time estimation and compensation keep  $i_d$  and  $i_q$  stable, preventing abrupt changes. The system utilizes the advantages of the super-twisting sliding mode to prevent oscillations during the adjustment process. Introducing a boundary layer function optimizes the system, enhancing control precision and robustness.

##### 4.1. Extended State Observer Design

As the current components  $i_d$  and  $i_q$  are symmetrical, we use the  $d$ -axis as an example for analysis. Considering the voltage drop, coupling terms, and back-EMF term as disturbances, we can redefine the equation as follows [21,22]:

$$\begin{aligned} \dot{i}_d &= d_d + b_d u_d \\ d_d &= b_d (-R i_d + \omega L i_q - u_{od}) + w \\ b_d &= 1/L \end{aligned} \quad (12)$$

where  $d_d$  represents the total disturbance on the  $d$ -axis. Let  $y = x_1 = i_d$ ,  $x_2 = d_d$ , and the  $d$ -axis state equation is modified as:

$$\begin{cases} \dot{x}(t) = Ax(t) + Bu_d(t) + Ed_d \\ y(t) = Cx(t) \end{cases} \quad (13)$$

$$\text{where } x = \begin{bmatrix} x_1 \\ x_2 \end{bmatrix}; A = \begin{bmatrix} 0 & 1 \\ 0 & 0 \end{bmatrix}; B = \begin{bmatrix} b \\ 0 \end{bmatrix}; C = [1 \ 0]; E = \begin{bmatrix} 1 \\ 0 \end{bmatrix}.$$

A new state observer is constructed to compensate for the disturbance terms in the system. This state observer can be designed as:

$$Z = A_z z(t) + B_z u_d(t) + L(y - \hat{z}_1) \quad (14)$$

where  $z = \begin{bmatrix} z_1 \\ z_2 \end{bmatrix}; A_z = A = \begin{bmatrix} 0 & 1 \\ 0 & 0 \end{bmatrix}; B_z = B = \begin{bmatrix} b \\ 0 \end{bmatrix}; L = \begin{bmatrix} l_1 \\ l_2 \end{bmatrix}$ .  $l_1$  and  $l_2$  are error gains, and by appropriately setting the parameters, this ensures the real-time tracking of  $z_1$  and  $z_2$  with respect to  $x_1$  and  $x_2$ . Derived from  $|sI_{2 \times 2} - (A - LC)| = (s + \omega_0)^n$ , the poles of the state observer are configured at the bandwidth  $\omega_0$ , i.e.,  $l_1 = 2\omega_0$ ,  $l_2 = \omega_0^2$ , where  $n$  is the order of ESO, which is equal to 2, and  $I_{2 \times 2}$  is the identity matrix of order  $2 \times 2$ . The only parameter of ESO is bandwidth, which is selected according to the convergence rate of ESO. The bandwidth of the observer is selected according to the maximum interference frequency of the system, and the resonance frequency of the system is regarded as the maximum interference frequency of the system.

#### 4.2. Improved Current Sliding Mode Controller Design

Our aim was to design an improved sliding mode control method for the current inner loop, reducing overshoot and oscillations in the system under input variations, and achieving fast steady-state response. Taking the  $d$ -axis as an example, the error  $e_d$  can be defined as follows:

$$e_d = i_{dref} - i_d \quad (15)$$

According to the requirements of the current inner loop control, the actual output current of the inverter needs to track the motion of the reference current. Set the sliding surface as

$$S_d = e_d + \lambda \int_0^t e_d dt \quad (16)$$

where  $\lambda$  is a proportionality term with a value greater than 0. When in sliding mode, the first-order derivative of the sliding surface is equal to 0. Taking derivatives on both sides of the sliding surface,

$$\dot{S}_d = \dot{e}_d + \lambda e_d = \dot{i}_{dref} - \dot{i}_d + \lambda e_d = 0 \quad (17)$$

Combining Equations (11), (15), and (17), the equivalent control law for  $d$ -axis is obtained:

$$u_{eqd} = L\dot{i}_{dref} + Ri_d - \omega Li_q + u_{od} + \lambda Le_d \quad (18)$$

When the system structure is known, using the equivalent control  $u_{eq}$  achieves control over the known part of the system. To suppress uncertainty disturbances, the switching control  $u_{st}$  is used. The  $d$ -axis control voltage is given by

$$u_d = u_{eqd} + u_{std} \quad (19)$$

An enhanced super-twisting sliding mode algorithm is designed to improve control precision for uncertainty disturbances. Express the traditional super-twisting sliding mode algorithm as follows:

$$\begin{cases} u_{STA} = \alpha |S|^{\frac{1}{2}} \text{sign}(S) + \chi \\ \dot{\chi} = \beta \text{sign}(S) \end{cases} \quad (20)$$

For this system, a modified boundary layer function is designed to optimize it:

$$\begin{cases} u_{\varepsilon STA} = \alpha |S|^{\frac{1}{2}} \text{sat}_1(S, \varepsilon) + \beta \int \text{sat}_2(S, \varepsilon) \\ \text{sat}_1(S, \varepsilon) = \begin{cases} \text{sign}(S) & |S| \geq \varepsilon \\ \frac{S}{\varepsilon^\gamma} & |S| < \varepsilon \end{cases} \end{cases} \quad (21)$$

where  $\alpha$  and  $\beta$  are control gains,  $0 < \varepsilon < 1$  is the boundary layer thickness, and  $\gamma > 1$  is the exponent factor. With the thickness value determined, introducing the exponent  $\varepsilon^\gamma$  improves control precision.

Let  $\phi_1$  be defined as  $\phi_1 = |s|^{1/2} \text{sat}_1(S, \varepsilon)$ . Taking its derivative, we can find

$$\text{sat}_2(S, \varepsilon) = \begin{cases} \text{sign}(S) & |S| \geq \varepsilon \\ \frac{|S|S}{\varepsilon^{2\gamma}} & |S| < \varepsilon \end{cases} \quad (22)$$

By substituting Equation (22) into Equation (21) and combining with Equations (18) and (19), we obtain the  $d$ -axis control voltage.

$$\begin{aligned} u_d &= u_{eqd} + u_{std} \\ &= L\dot{i}_{dref} + Ri_d - \omega Li_q + u_{od} + \lambda Le_d + \alpha_1 |S_d|^{\frac{1}{2}} \text{sat}_1(S_d, \varepsilon) + \beta_1 \int \text{sat}_2(S_d, \varepsilon) \end{aligned} \quad (23)$$

Similarly, the  $q$ -axis control voltage is obtained as well.

$$\begin{aligned} u_q &= u_{eqq} + u_{stq} \\ &= L\dot{i}_{qref} + Ri_q + \omega Li_d + u_{oq} + \lambda Le_q + \alpha_2 |S_q|^{\frac{1}{2}} \text{sat}_1(S_q, \varepsilon) + \beta_2 \int \text{sat}_2(S_q, \varepsilon) \end{aligned} \quad (24)$$

#### 4.3. Design and Stability Analysis of the Combined Control System

Combining the ESO with the improved sliding mode controller forms a composite control system. The observer compensates for disturbances through disturbance estimation, and the enhanced super-twisting sliding mode controller tracks errors. Combining Equations (12) and (15) gives the compensated  $d$ -axis voltage after applying the extended state observer:

$$\begin{aligned} u_d &= \frac{1}{b_d} \left[ \dot{i}_{dref} - x_2 + \lambda (i_{dref} - x_1) + \alpha_1 b_d |S_d|^{\frac{1}{2}} \text{sat}_1(S_d, \varepsilon) + \beta_1 b_d \int \text{sat}_2(S_d, \varepsilon) \right] \\ &= \frac{1}{b_d} \left[ \dot{i}_{dref} - z_2 + \lambda (i_{dref} - z_1) + \alpha_1 b_d |S_d|^{\frac{1}{2}} \text{sat}_1(S_d, \varepsilon) + \beta_1 b_d \int \text{sat}_2(S_d, \varepsilon) \right] \end{aligned} \quad (25)$$

The composite control structure is illustrated in Figure 7.

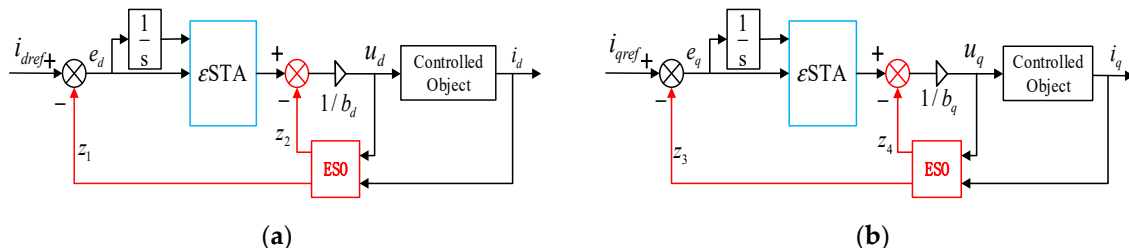


**Figure 7.** ESO +  $\varepsilon$ STA control diagram: (a)  $d$ -axis, (b)  $q$ -axis.

To verify the stability of the system, define the Lyapunov function as  $V = 0.5S^T S$ . For the system to operate stably, its derivative should be less than 0. Take the derivative as follows:

$$\begin{aligned}\dot{V} &= \frac{1}{2}S^T \dot{S} = S_d \dot{S}_d + S_q \dot{S}_q \\ &= S_d \left( i_{dref} + \lambda(i_{dref} - z_1) - b_d u_d - z_2 \right) + S_q \left( i_{qref} + \lambda(i_{qref} - z_3) - b_q u_q - z_4 \right) \\ &= S_d \left( -\alpha_1 |S_d|^{\frac{1}{2}} \text{sat}_1(S_d, \varepsilon) - \beta_1 \int \text{sat}_2(S_d, \varepsilon) \right) + S_q \left( -\alpha_2 |S_q|^{\frac{1}{2}} \text{sat}_1(S_q, \varepsilon) - \beta_2 \int \text{sat}_2(S_q, \varepsilon) \right) \\ &= - \left( \alpha_1 |S_d|^{\frac{1}{2}} S_d \text{sat}_1(S_d, \varepsilon) + \alpha_2 |S_q|^{\frac{1}{2}} S_q \text{sat}_1(S_q, \varepsilon) + \beta_1 S_d \int \text{sat}_2(S_d, \varepsilon) + \beta_2 S_q \int \text{sat}_2(S_q, \varepsilon) \right) \\ &< 0\end{aligned}\quad (26)$$

Outside the boundary layer  $\varepsilon$ , the improved control rate sat remains the sign function, and its performance is consistent with the traditional super-twisting sliding mode. Within the boundary layer, the sign of the sat function aligns with  $S$ . Therefore, by ensuring  $\alpha_1, \alpha_2 > 0$  and  $\beta_1, \beta_2 > 0$ , the system can maintain stability. Through the computer simulation, to select the appropriate parameters, after many simulation comparisons, it was found that  $\alpha_1, \alpha_2$  is smaller, the system's response speed is slower, and the value is too large to affect the system stability, and the larger the value of  $\beta_1, \beta_2$ , the shorter the time for the system to move towards the sliding mode surface, but the larger the value of  $\beta_1, \beta_2$ , the more unstable the system will be. The optimal values for  $\alpha_1, \alpha_2, \beta_1, \beta_2$  require iterative experiments to determine.

### 5. Simulation and Analysis of Microgrid Operation Mode Switching

To validate the control performance of the proposed smooth switching composite control system, a system model was constructed using the Matlab/Simulink (R2021b) platform. The study focused on grid-connected/islanded transitions and islanded/grid-connected transitions, with the conventional status follower VSG/PQ used for comparison. The microgrid model comprises a PCS, a filtering circuit, two sets of loads, and the main power grid. Tables 1 and 2 present simulation parameters and control system parameter settings. During islanded operation, set the active power to 45 kW and the reactive power to 10 kvar. During grid-connected operation, set the active power to 55 kW and the reactive power to 10 kvar.

**Table 1.** Electrical parameter settings.

Symbol	Instruction	Values
$U_{dc}$	DC voltage	800 V
$u_g$	Grid voltage	380 V
$f_n$	Grid frequency	50 Hz
$L_g$	Grid side inductance	2.5 mH
$J$	Rotational inertia	0.3 J/kg·m <sup>2</sup>
$D$	Damping coefficient	10 N·m·s/rad
$f_s$	Switch frequency	5 kHz
$L$	Inverter inductance	5 mH
$C$	Filter capacitor	20 μF
$R$	Equivalent resistance	0.2 Ω

**Table 2.** Control parameter settings.

Symbol	Values
$l_1$	6000
$l_2$	800,000
$\varepsilon$	20
$\lambda$	200,000
$\alpha_1$	500

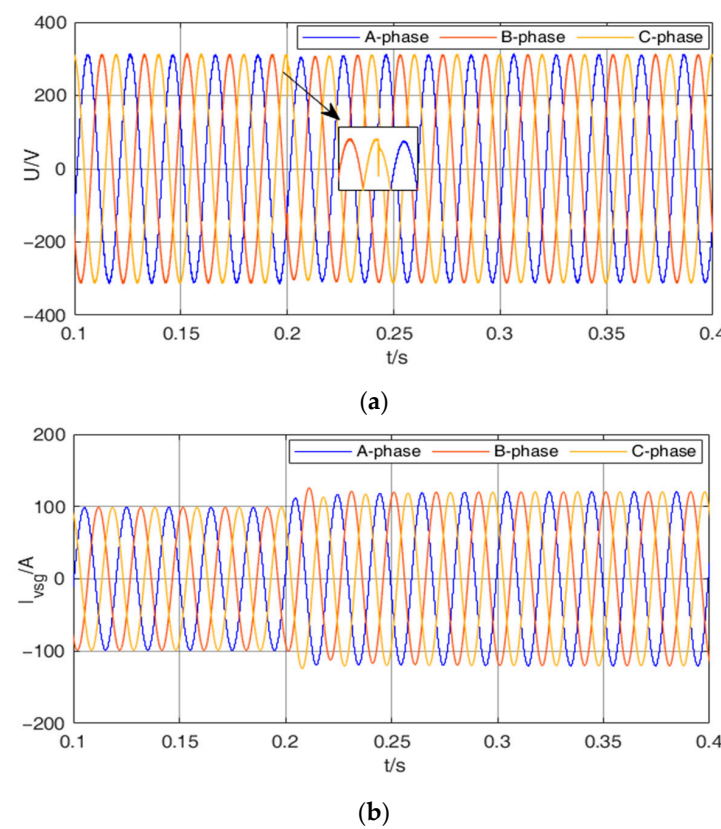
**Table 2.** Cont.

Symbol	Values
$\alpha_2$	400
$\beta_1$	1000
$\beta_2$	15,000
$\gamma_1$	2
$\gamma_2$	2.8

### 5.1. Simulation of Islanded Switching to Grid-Connected Switching

At the initial moment, the microgrid operates in islanded mode, and the PCS, adopting the VSG control strategy, supports a load of 45 kW of active power and 10 kvar of reactive power. At  $t = 0.2$  s, the pre-synchronization begins, and both VSG and PQ control strategies run simultaneously. After completing the pre-synchronization, the microgrid switches to grid-connected mode. To validate the correctness of the proposed strategy, the PCS, upon grid connection, takes on the microgrid load and simultaneously feeds 10 kW of active power to the grid. The simulation results are shown in Figures 8 and 9, where  $U$  represents the grid voltage,  $I_{vsg}$  is the filtered microgrid current, and  $I_{grid}$  is the grid current.

From Figure 8, it is evident that conventional islanded/grid-connected switching results in a certain degree of voltage distortion when transitioning from islanded to grid-connected mode. Additionally, it leads to power fluctuations and significant transient currents, with a longer adjustment time. As shown in Figure 9, adopting the improved method proposed in this paper for islanded/grid-connected switching, pre-synchronization adjustment begins immediately upon receiving the signal at 0.2 s. After the pre-synchronization of the microgrid voltage and frequency is completed, around 0.225 s, grid connection is initiated without voltage fluctuations or current surges, and power fluctuations are minimal. The improved control strategy effectively reduces the impact during microgrid mode transitions, thereby enhancing the quality of electrical energy.

**Figure 8.** Cont.

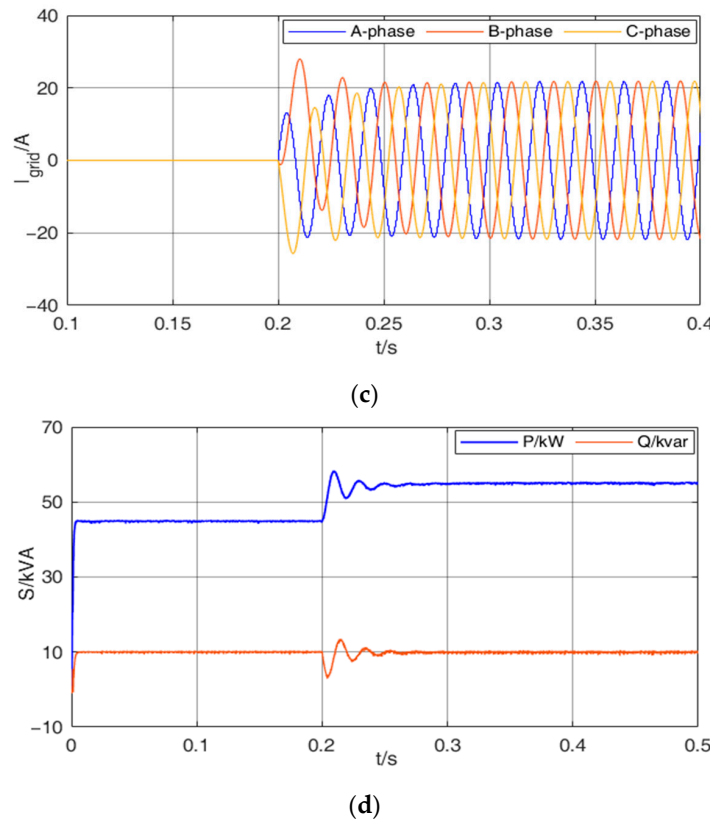


**Figure 8.** Simulation results of conventional switching from islanded to grid-connected modes. (a) PCS output voltage waveform, (b) PCS output current waveform, (c) PCC grid side current waveform, (d) PCS output power waveform.

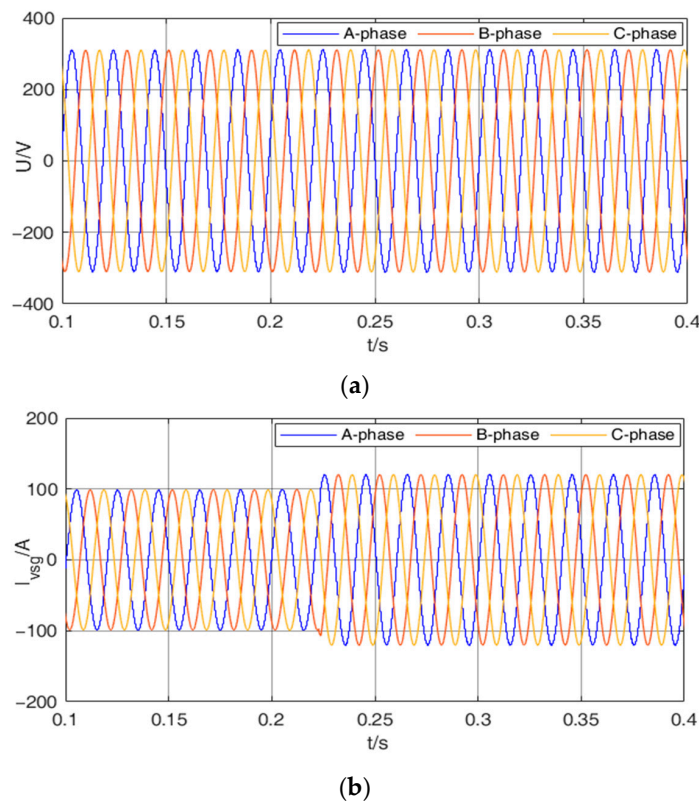


**Figure 9. Cont.**

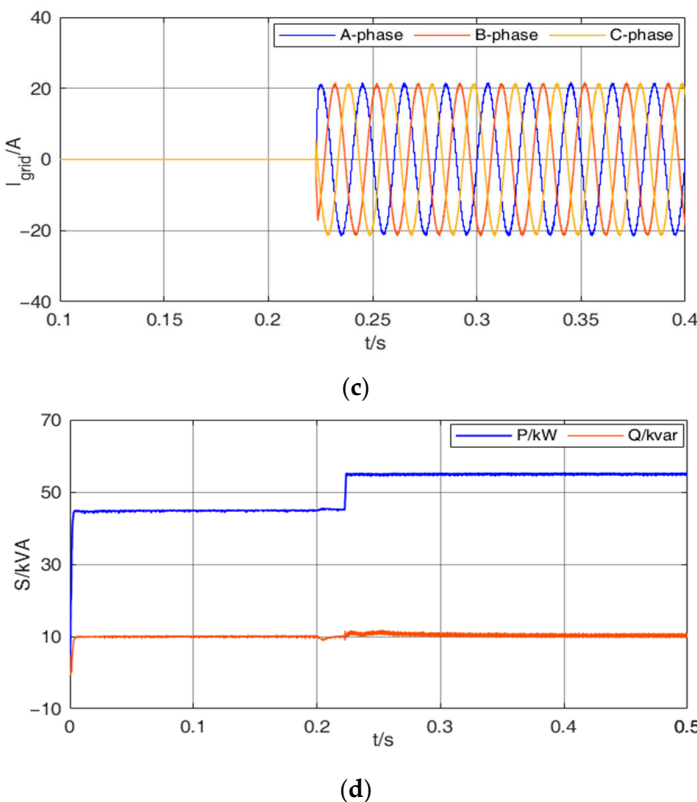


**Figure 9.** Simulation results of improved switching from islanded to grid-connected mode. (a) PCS output voltage waveform, (b) PCS output current waveform, (c) PCC grid side current waveform, (d) PCS output power waveform.

### 5.2. Simulation of Switching from Grid to Island

Before 0.7 s, the microgrid was initially in grid-connected operation with an active load of 55 kW and a reactive load of 10 kvar. At  $t = 0.7$  s, a fault occurred in the main grid, leading to an immediate transition to islanded operation. During islanded operation, the VSG supplied an active power of 45 kW and a reactive power of 10 kvar. For comparison, we used conventional dual-mode operation with grid/island switching as the control group. The simulation results are presented in Figures 10 and 11.

As shown in Figure 10, conventional grid/island switching results in a slight decrease in voltage magnitude during the transition from grid-connected to island operation. The output current from the PCS and the current from the main grid exhibit significant shocks, leading to considerable overshoot and adversely affecting the microgrid load's stable operation. In contrast, as depicted in Figure 11, employing the improved method proposed in this paper for grid-connected/islanded switching maintains a nearly constant microgrid voltage, and the microgrid current shows no overshoot or oscillations, avoiding any impact on the load stability.

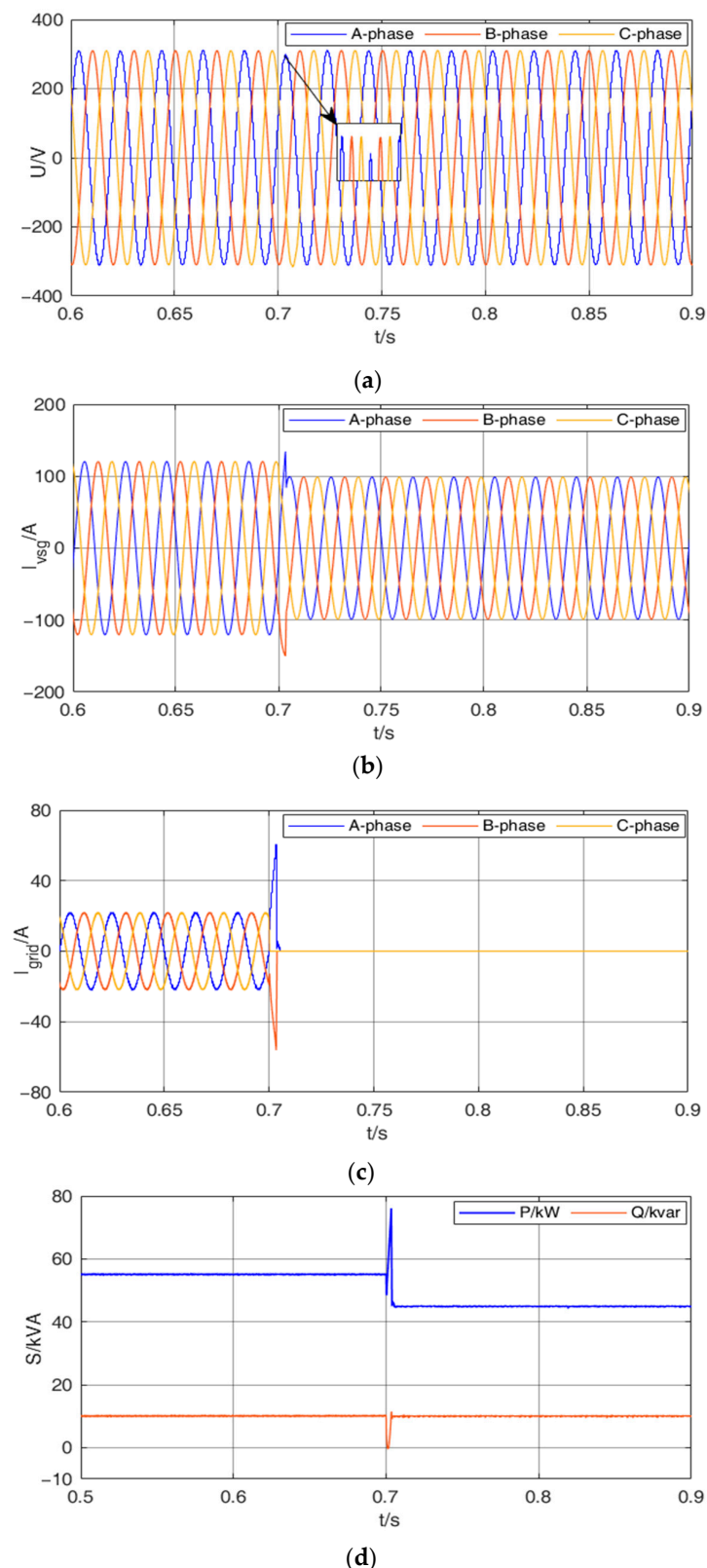


**Figure 10.** Simulation results of conventional switching from grid-connected to islanded mode. **(a)** PCS output voltage waveform, **(b)** PCS output current waveform, **(c)** PCC grid side current waveform, **(d)** PCS output power waveform.

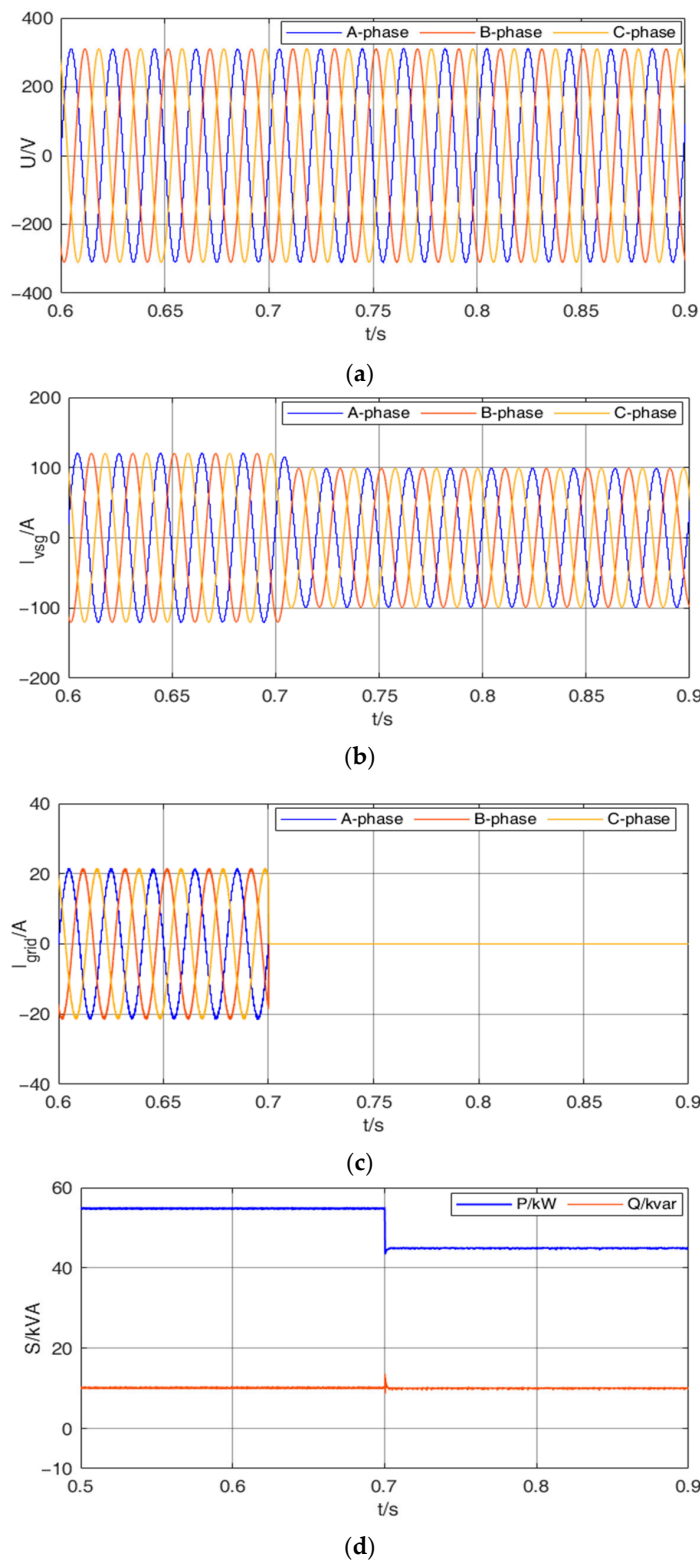


**Figure 11.** Simulation results of improved switching from grid-connected to islanded mode. (a) PCS output voltage waveform, (b) PCS output current waveform, (c) PCC grid side current waveform, (d) PCS output power waveform.

## 6. Experimental Results

In order to verify the accuracy and reliability of the above theory, an experimental platform was built, as shown in Figure 12. The main circuit and the control loop model

were built for the optical storage AC microgrid. The main circuit makes the photovoltaic power generation system, the PCS and the load adopt the common AC bus structure, integrated with TI's TMS320F28355 DSP and oscilloscope. Both photovoltaic and energy storage batteries have DC sources instead. Table 3 present the experimental parameters.



**Figure 12.** Physical representation of the experimental prototype.

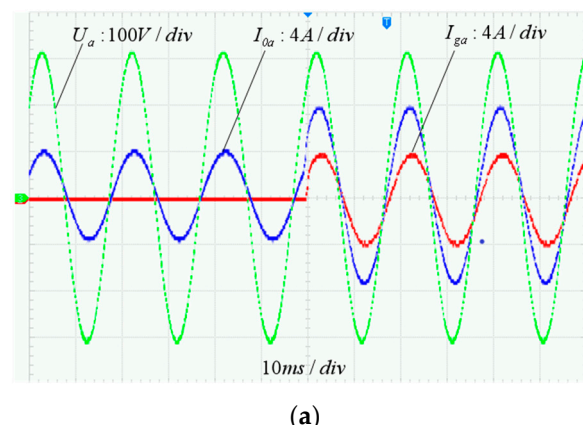
**Table 3.** System parameter settings.

Symbol	Instruction	Values
$U_{dc}$	DC voltage	500 V
$u_g$	Grid voltage	380 V
$f_n$	Grid frequency	50 Hz
$f_s$	Switch frequency	5 kHz

### 6.1. Scenario 1

At the initial time, the micro-grid is off-grid, and the load is a pure active load of 4 kW. At same time, the active power output of the photovoltaic system is 2 kW, the power output of the PCS is 2 kW, and the VSG control strategy is used. At micro-grid pre-synchronization, VSG and PQ run side by side, and the micro-grid switches to the on-grid after pre-synchronization. PQ control is used in grid-connected operation. The output power is 4 kW, and 2 kW of it flows into the large power grid.

When the micro-grid is on-grid, the load is switched from 4 kW to 3 kW. The output power of the PCS is still 4 kW, and 3 kW of it flows into the large power grid. When the reference power of the PQ control of the PCS changes suddenly, the reference power changes from 4 kW to 3 kW. The output power of the PCS is 3 kW, and 2 kW of it flows into the large power grid. The output voltage and the current of the PCS, and the grid side current, are shown in Figure 13. Taking Phase A as an example,  $U_a$  is the output voltage of the PCS,  $I_{0a}$  is the output current of the PCS, and  $I_{ga}$  is the grid side current.



(a)

**Figure 13.** Cont.

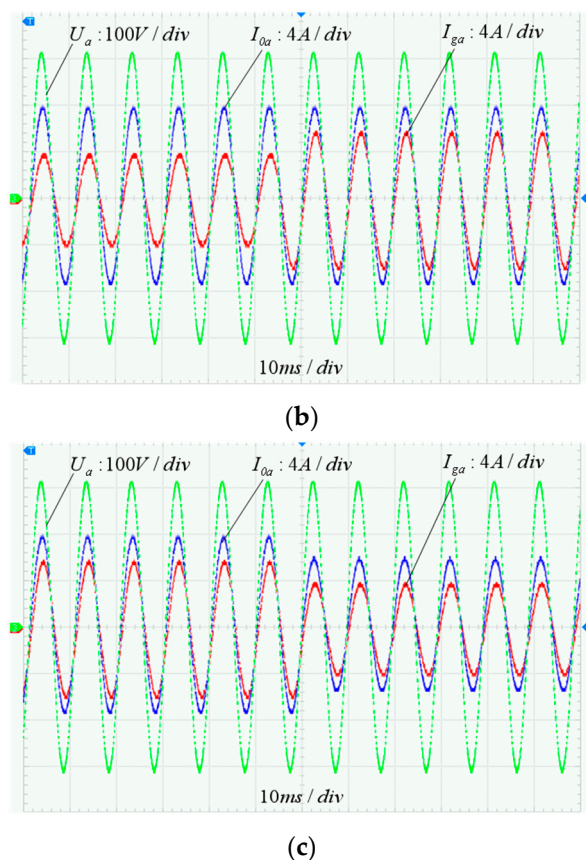


**Figure 13.** Output waveform magnification diagram of PCS. (a) Off-grid/on-grid switching waveform magnification diagram of PCS, (b) magnification of the waveform when the load changes suddenly, (c) magnification of the waveform when the reference power changes.

As shown in Figure 13, when the new control strategy is adopted, the voltage of the PCS can be kept stable and the current can be switched quickly without impact on the large power grid. If the PCS works in grid-connected mode, it can respond quickly when the load is suddenly cut off or the reference power is changed.

#### 6.2. Scenario 2

At the initial time, the micro-grid is on-grid, and the load is a pure active load of 4 kW. The active power output of the photovoltaic system is 2 kW. The reference power of PCS's PQ control is 3 kW, and 1 kW of it flows into the large power grid. When the system is switched to off-grid, the PCS adopts the VSG control strategy and the reference output power is 2 kW. When the micro-grid is off-grid, the load is cut off from 4 kW to 3 kW. The output voltage, current, and current of the PCS are shown in Figure 14. Taking Phase A as an example,  $U_a$  is the output voltage,  $I_{0a}$  is the output current, and  $I_{ga}$  is the grid side current.

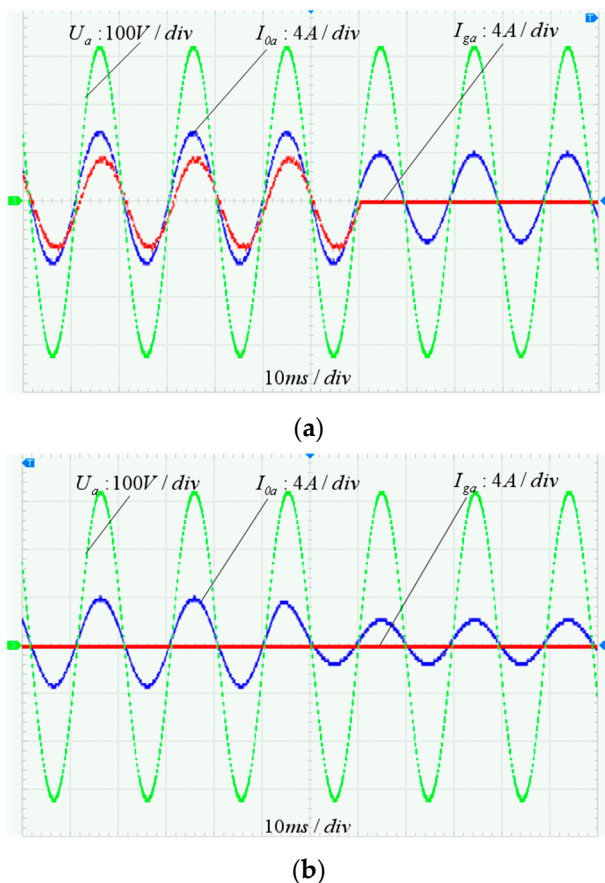


**Figure 14.** Output waveform magnification diagram of PCS. (a) On-grid/off-grid switching waveform magnification diagram of PCS, (b) magnification of the waveform when the load changes suddenly.

As shown in Figure 14, when the new control strategy is adopted, the voltage of the PCS can be kept stable, the current can be switched quickly, no clutter is produced, and the power grid is not impacted. If the micro-grid is in off-grid operation mode, the output voltage of the PCS does not increase or decrease suddenly because of the load fluctuation, and the voltage and current will be in a stable operating state.

## 7. Conclusions and Future Perspectives

In this study, a novel method is proposed that integrates the super-twisting control algorithm with an extended state observer. Enabling the simultaneous operation of VSG control and PQ control in the PCS, and sharing the inner current loop, facilitates the transition between control strategies through the transformation of control signals. The combination of the super-twisting control algorithm and an extended state observer effectively addresses reference signal issues during the switching process, thereby improving its dynamic performance. The simulation and experimental results show that the control strategy can achieve the stable operation of the micro-network with the least influence during the switching process. The following conclusions are derived:

- (1) The introduction of an improved boundary layer super-twisting control algorithm into the current inner loop control of the PCS enhances system robustness, rapid response, and operational stability.
- (2) The super-twisting control algorithm and an extended state observer are used together to improve the system's dynamic performance and deal with the problem of sudden changes in current commands during microgrid islanding and grid-connected switching. During control signal switching, the voltage and current changes are smoother, reducing the impact on power.

- (3) This study focuses on PCS and considers only the islanding/grid-connected switching under energy storage. Further research is necessary for the coordinated management of multiple inverters within the system.

**Author Contributions:** Conceptualization, J.K. and Y.W.; methodology, J.K.; software, Y.W.; validation, J.W.; formal analysis, Y.W.; investigation, Y.W.; resources, B.L.; data curation, Y.W.; writing—original draft preparation, Y.W.; writing—review and editing, Y.W.; visualization, J.W.; supervision, J.K.; project administration, B.L.; funding acquisition, J.K. All authors have read and agreed to the published version of the manuscript.

**Funding:** This work was supported by the Key R&D Program of Shaanxi Province, China (2021GY-135) and the Natural Science Foundation of Shaanxi Province, China (2023-JC-YB-381).

**Data Availability Statement:** Data are contained within the article.

**Conflicts of Interest:** The authors declare no conflicts of interest.

## Abbreviations

The following abbreviations are used in this manuscript:

ESO	Extended State Observer
STA	Super-Twisting Algorithm
VSG	Virtual Synchronous Generator
PCS	Power Conversion System
PCC	Point of Common Coupling
DC	Direct Current
AC	Alternating Current
SPWM	Sinusoidal Pulse Width Modulation

## References

1. Liu, M.; Wang, S.; Wen, S. Research on smooth off-grid switching control strategy for optical storage micro-grid. *Renew. Energy Resour.* **2020**, *38*, 1633–1639.
2. Zhu, Z.; Sun, S.; Ding, Y.; Huang, S. Research on Control Strategy of Hybrid Energy Storage System with Optical Storage Microgrid. *J. Electr. Eng. Technol.* **2020**, *18*, 2835–2845. [[CrossRef](#)]
3. Liu, X.; Wang, S.; Song, X.; Zhou, J. Stability Control Strategies for Bidirectional Energy Storage Converters Considering AC Constant Power Loads. *Electronics* **2023**, *12*, 1067. [[CrossRef](#)]
4. Javed, K.; Vandevelde, L.; De, B. Analysis and Demonstration of Control Scheme for Multiple Operating Modes of Energy Storage Converters to Enhance Power Factor. *Mathematics* **2022**, *10*, 3434. [[CrossRef](#)]
5. Guo, P.; Xu, Q.; Yue, Y.; Ma, F.; He, Z. Analysis and Control of Modular Multilevel Converter With Split Energy Storage for Railway Traction Power Conditioner. *IEEE Trans. Power. Electron.* **2020**, *35*, 1239–1255. [[CrossRef](#)]
6. Guo, L.; Xu, Z.; Jin, N.; Li, Y.; Wang, W. A Weighted Voltage Model Predictive Control Method for a Virtual Synchronous Generator with Enhanced Parameter Robustness. *Prot. Control Mod. Power Syst.* **2021**, *6*, 482–492. [[CrossRef](#)]
7. Huang, H.; Zhou, M.; Li, G. An endogenous approach to quantifying the wind power reserve. *IEEE Trans. Power Syst.* **2020**, *35*, 2431–2442. [[CrossRef](#)]
8. Hu, S.; Yuan, X.; Zhu, Y.; Gao, Z.; Li, Z. Research on seamless switching control technology of microgrid operation mode. *Elect. Meas. Instrum.* **2018**, *55*, 56–61.
9. Chen, J.; Chen, X.; Feng, Z.; Gong, C.; Yan, Y. Seamless switching control strategy of grid-connection/islanding operation mode of microgrid system. *Proc. CSEE* **2014**, *34*, 3089–3097.
10. Ma, H.; Zhou, B.; He, Y.; Bai, H.; Li, F. Study on seamless handoff control strategy of microgrid. *Smart Power.* **2020**, *5*, 53–59.
11. Shi, R.; Zhang, X.; Xu, H.; Liu, F.; Cao, W. Virtual synchronous generator power control strategy based on adaptive mode switching. *Trans. China Electrotechnical. Soc.* **2017**, *32*, 127–137.
12. Wang, H.; Hao, Z.; Chen, Z.; Chen, X.; Teng, F.; Kong, D. Control strategy of energy storage inverter based on virtual synchronous generator and seamless switching technology. *Sci. Technol. Eng.* **2022**, *22*, 3594–3600.
13. Li, Y.; Cao, S.; Shi, W. Integrated Control Strategy for Smooth Switching of the PV and Battery-storage Micro-grid Based on Operation State Tracking. *J. Eng.* **2019**, *16*, 1062–1067.
14. Kang, J.; Chai, Y.; Cao, J.; Wang, S. Research on grid-connected PV control strategy based on improved sliding mode control. *Renew. Energy Resour.* **2019**, *1*, 59–64.
15. Gao, L.; Zhao, X.; Song, L.; Wang, Y. Control strategy of photovoltaic grid-connected inverter based on sliding mode control. *Autom. Instrum.* **2022**, *37*, 37–43.

16. Vo, A.; Kang, H. An adaptive terminal sliding mode control for robot manipulators with non-singular terminal sliding surface variables. *IEEE Access* **2019**, *7*, 8701–8712. [[CrossRef](#)]
17. Ramezani, M.; Li, S.; Musavi, F.; Golestan, S. Seamless Transition of Synchronous Inverters Using Synchronizing Virtual Torque and Flux Linkage. *IEEE Trans. Ind. Electron.* **2020**, *67*, 319–328. [[CrossRef](#)]
18. Koiwa, K.; Inoo, K.; Liu, K.; Zanma, T. Current analysis of grid-connected Inverter with VSG controller under voltage dip and recovery. *IEEJ Trans. Electr. Electron. Eng.* **2020**, *15*, 1698–1700. [[CrossRef](#)]
19. Liang, J.; Fan, H.; Cheng, L. Control strategy for improving the frequency response characteristics of photovoltaic and energy storage systems based on VSG control. *Energy Rep.* **2024**, *11*, 2295–2305. [[CrossRef](#)]
20. Feng, J.; Zhuang, X. Enhancement of low-voltage ride-through capability for virtual synchronous generators based on virtual impedance voltage control. *Energy Rep.* **2023**, *9*, 406–415.
21. Saleem, M.; Choi, K.; Kim, R. Resonance damping for an LCL filter type grid-connected inverter with active disturbance rejection control under grid impedance uncertainty. *Electr. Power Energy Syst.* **2019**, *109*, 444–454. [[CrossRef](#)]
22. Zhou, W.; Su, S.; Su, J.; Ouyang, Z. Improved Sliding Mode Voltage Stability Control of Bidirectional AC/DC Converter in AC/DC Microgrid Based on NLESO. *Power Capacitor. React Power Compens.* **2023**, *44*, 150–157.

**Disclaimer/Publisher’s Note:** The statements, opinions and data contained in all publications are solely those of the individual author(s) and contributor(s) and not of MDPI and/or the editor(s). MDPI and/or the editor(s) disclaim responsibility for any injury to people or property resulting from any ideas, methods, instructions or products referred to in the content.